

**Fig. 5.2:** A sample acoustic radiation force distribution shown with a schematic of the lesion's location and size in the simulated tissue domain. Note how the focal point is adjacent to the lesion, offset in this case by 1.25 cm. The focal line extends laterally from the focal point, through the lesion, to the edge of the tissue domain—this is the line that will be used to calculate shear wave speeds.

Lamé's second parameter for the lesion and tissue respectively,  $c_{T,l}$  and  $c_{T,t}$  are the shear wave speeds in the lesion and tissue respectively, and  $\rho$  is the density of the tissue and assumed to be constant between the lesion and tissue.

$$c_T = \sqrt{\frac{\mu}{\rho}} \quad (5.12a)$$

$$c_T^2 \rho = \mu \quad (5.12b)$$

$$E_{rel} = \frac{\mu_l}{\mu_t} = \left( \frac{c_{T,l}}{c_{T,t}} \right)^2 \quad (5.12c)$$

In order to determine the velocity of generated shear waves, the ARFI load-induced displacement of the soft tissue must be tracked through time along a line passing through the focal point radiating laterally outward in the finite-element model of tissue deformation. A sample result of tissue displacement

through time and along such a line is presented in Fig. 5.3 where the wave can be readily visualized through time, noting that the wave travels ever further from the centreline.

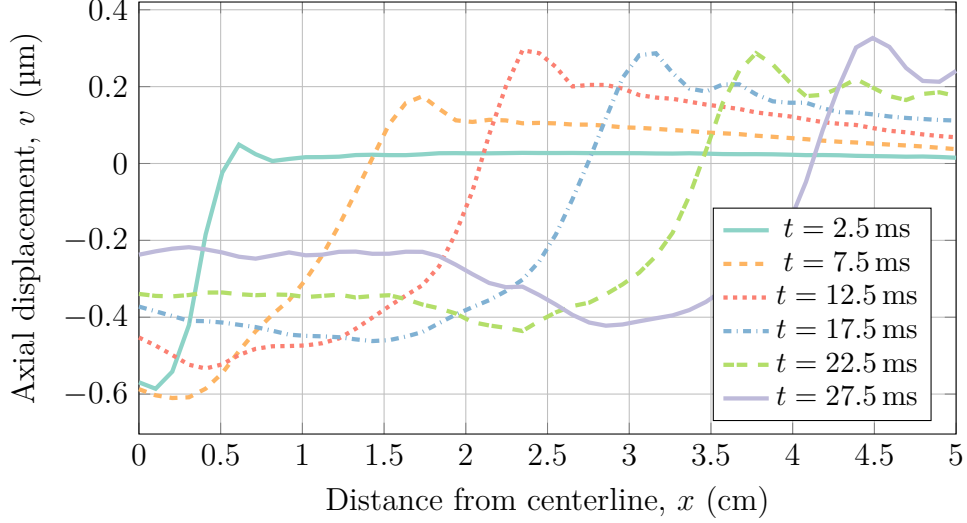


**Fig. 5.3:** Axial displacement induced by a shear wave traveling laterally across the focal line of an ARFI load. There is a stiff ( $E_{rel} = 3.2$ ) lesion with a diameter of 1 cm located 1.25 cm away from the centerline, with both the focal line and the lesion located at a depth of 4 cm from the surface.

The results in Fig. 5.3 represent a finite subsample of the shear wave's propagation along the focal line. For a continuous representation of the shear wave propagation, the surface shown in Fig 5.4 may be constructed. In order to track the wave through both position and time, a contour line representing a constant displacement value may be extracted. For this work, a contour line representing the mean value of the displacement over the entire position-time domain was utilized and is portrayed in Fig. 5.5.

Fig. 5.6 represents the extracted contour line. This contour line now represents a position-time trace of the shear wave, from which the velocity of the wave may be calculated by differentiating the position of the wave with respect to time as per equation 5.13. Care must be taken when numerically

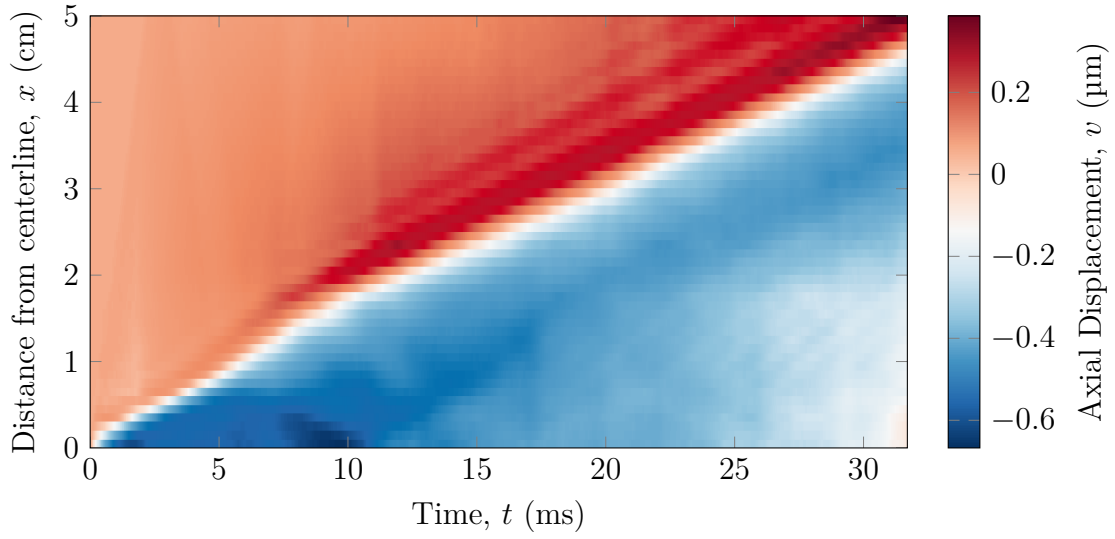


**Fig. 5.4:** Continuous surface plot of the shear wave induced axial displacement tracked through both time and distance from the transducer centreline. The sharp transition from negative to positive displacement marks the location of shear wave in time at any given location.

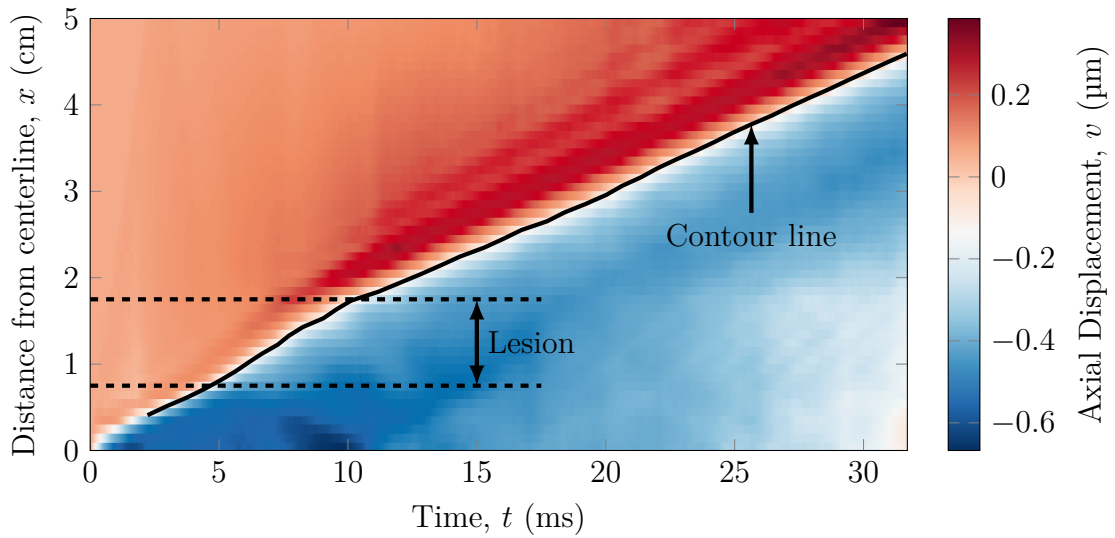


**Fig. 5.5:** Continuous surface plot of shear wave induced axial displacement highlighting a mean contour line representing the shear wave location as time progresses. By inspection, the slope of the contour line is greater within the lesionous region than outside of it, suggesting that the lesion is stiffer than the surrounding tissue.

differentiating, as numerical errors are greatly amplified by differentiation. To combat this, a moving window average filter with a kernel of 5 mm was applied

to the position-time curve before centre-difference differentiation was used to result in the shear wave speed graph given in Fig. 5.7. Sample source code used to extract and generate the shear wave speed plot is given in listing B.6 in Appendix B.

$$c_T = \frac{dx}{dt} \quad (5.13)$$

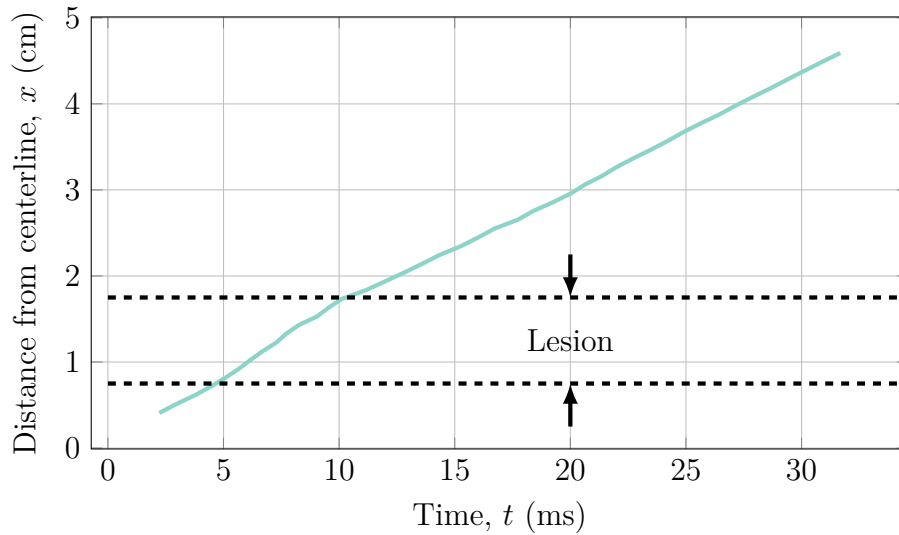


**Fig. 5.6:** The extracted shear wave position-time trace showing the location of the generated shear wave increases with time, albeit at different rates depending on the underlying tissue properties.

As is shown in Fig. 5.7, the speed of the shear wave within the lesion (which was in this case 3.2 times as stiff as the surrounding tissue) is substantially greater than the shear wave speed in the regular tissue. Note that instead of an impulse response at the boundaries of the lesion as might be expected, the shear wave speed reaches a peak value approximately halfway through the lesion, indicating that the wave requires some finite amount of time to both speed up and slow down within the lesion, suggesting that the technique may have difficulty identifying small lesions as the shear wave speed will not be

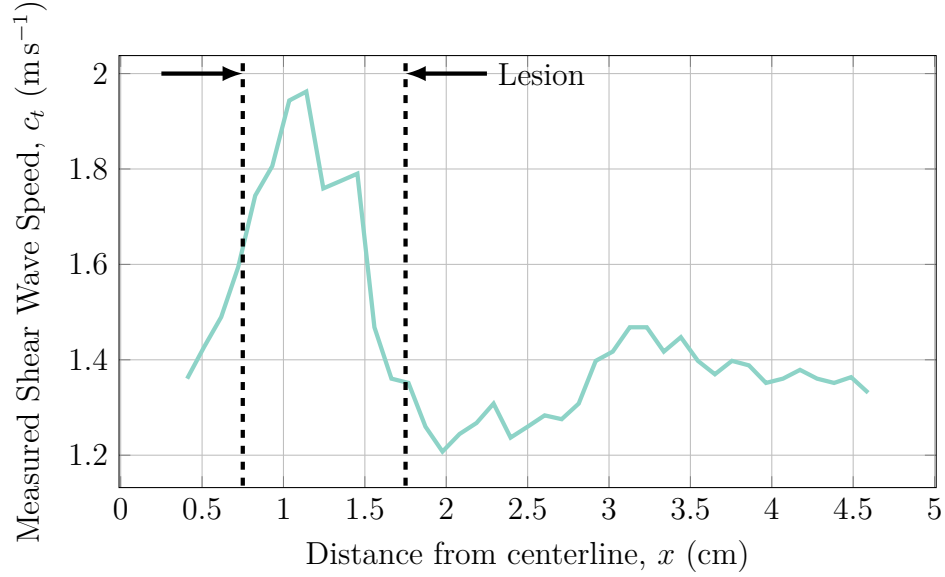


**Fig. 5.7:** Trace of the shear wave speed along the focal line through both lesionous and “healthy” tissue. The shear wave speed within the lesion is much greater than the shear wave speed through the “healthy” tissue, indicating that the lesion is significantly stiffer than the surrounding tissue. The shear wave speed was calculated as the numerical differentiation of the shear wave’s position through time.

able to fully adjust to the lesion in the time it takes for the wave to completely pass through the lesion.

### 5.3.3 Lesion Detection Characterization

In order to determine the detection sensitivity of shear wave speed quantification with respect to lesion size, hard-boundaried spherical lesions with varying radii were interrogated using ARFI loads while the speed of the shear waves developed along the focal line were monitored. The ARFI loads were applied using a probing frequency of 2 MHz for 150  $\mu$ s with a source pressure of 3.35 MPa using an F-number of  $f/1.0$ . The lesions were located at a depth of 4 cm with an offset of 1.25 cm from the focal point of the ARFI load. The results of this characterization are given in Fig. 5.8. Lesions stiffness ratios

were measured by calculating the maximum or minimum shear wave speed within the lesion if the shear wave speed within the lesion was greater than or less than the surrounding tissue respectively and the mean shear wave speed without the lesion and applying equation 5.10.

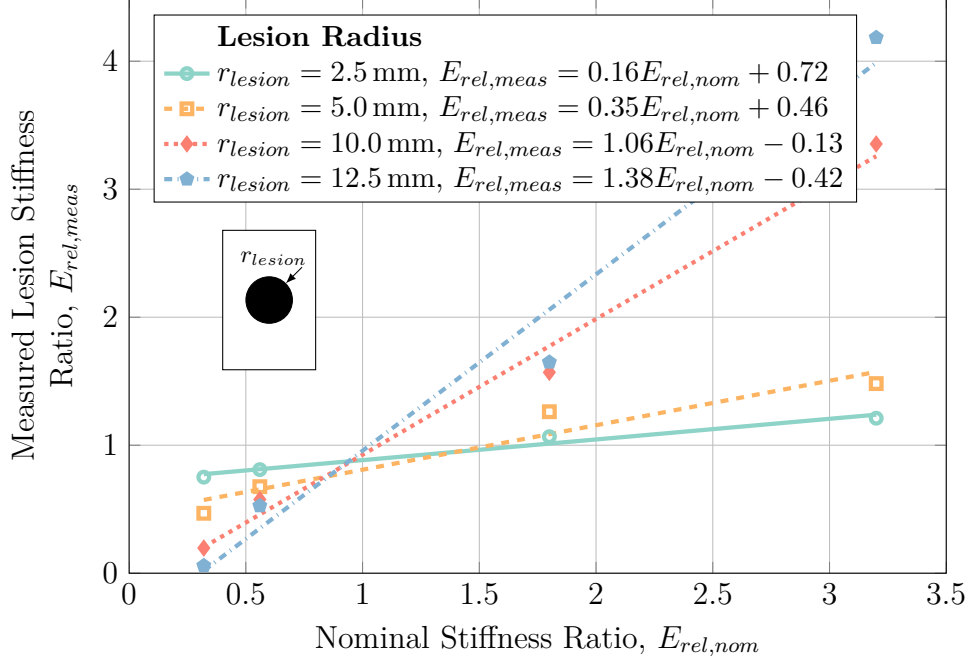


**Fig. 5.8:** Numerical characterization of the shear wave speed measured stiffness ratios acquired with varying lesion radii for a hard-boundaried lesion at a depth of 4 cm using an ARFI interrogation frequency of 2 MHz.

As can be seen in Fig. 5.8, small lesions with radii  $\leq 5.0$  mm are nearly impossible to detect—large changes in the true lesion stiffness ratio represent very minute changes in the measured lesion stiffness ratio for these small lesions. Conversely, large lesions are much easier to detect, portraying a nearly one-to-one or better mapping between the true and measured lesion stiffness ratios. This suggests that the larger a lesion is, the more readily it may be detected while smaller lesions are more difficult to detect with a lower limit of the lesion radius approaching 5.0 mm.

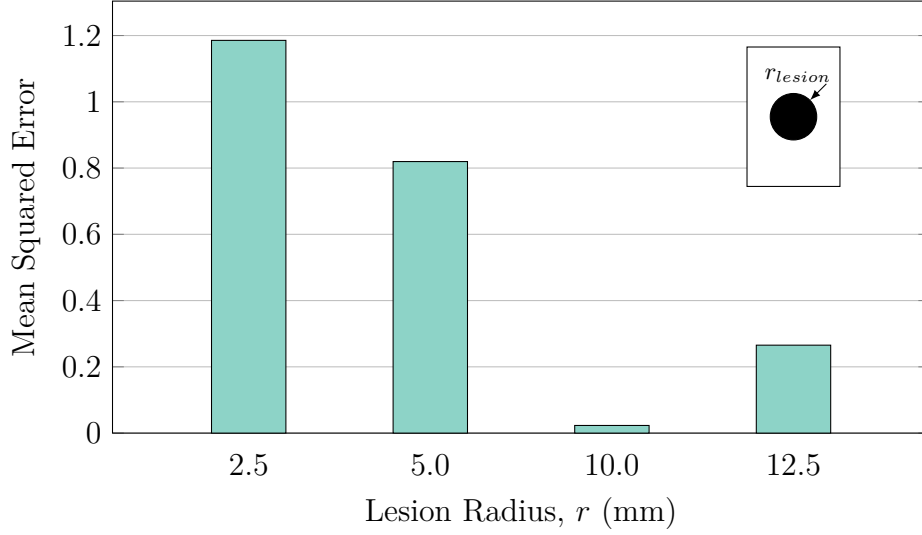


**Fig. 5.9:** Mean squared error between the true and measured lesion stiffness ratios for increasing lesion radii for a hard-boundaried lesion at a depth of 4 cm using an ARFI interrogation frequency of 2 MHz.

To further investigate these results, the mean-squared error associated with varying lesion size was calculated as per equation 4.17 with the results presented in Fig. 5.9. In Fig. 5.9, it is clear to see that the error associated with small lesions was significantly greater than with larger lesions. Interestingly, the largest lesions tested (with radii of 12.5 mm) presented greater error than lesions with radii of 10.0 mm. This increase in error may be largely attributed to the over-estimation of the lesion stiffness ratio for a stiff ( $3.2 \times$  basal stiffness) lesion with a radius of 12.5 mm seen in Fig. 5.8.

One of the key parameters used in shear wave speed quantification is the distance between the focal point of the acoustic radiation force and the lesion itself. In order to adequately generate fully-formed shear waves within the lesion, the focal point of acoustic radiation force should be located adjacent to the lesion. As can be seen in Fig. 5.10, regardless of the lesion offset distance, shear wave speed quantification is able to differentiate lesions from the tissue

with reasonable accuracy. The largest exception to this generalization is for very stiff lesions for which the ARFI load is focused the farthest away from the lesion. It is hypothesized that the measured stiffness ratio of these lesions is underestimated because by the time the shear wave reaches the relatively far-away lesion, it's energy has substantially dissipated, disallowing the wave to remain fully cohesive and speed up appropriately.

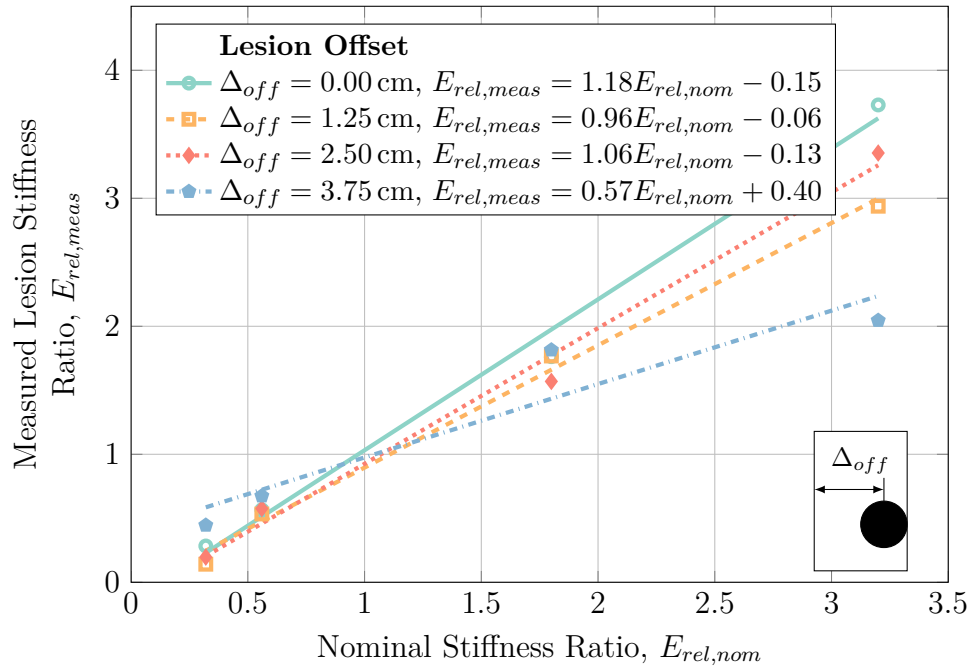


**Fig. 5.10:** Numerical characterization of the shear wave speed measured stiffness ratios acquired with varying lesion offsets for a hard-boundaried 0.5 cm radius lesion at a depth of 4 cm using an ARFI interrogation frequency of 2 MHz. The greatest error between the true and measured stiffness ratios occurred at the highest stiffness ratio of 3.2, with the large lesion offset underestimating the stiffness ratio and the negated lesion offset overestimating the stiffness ratio.

Fig. 5.11 portrays the mean squared error between the measured and true lesion stiffness ratios with increasing lesion offset distance. As Fig. 5.11 shows, a lesion offset of approximately 2.5 cm is ideal for quantifying lesion stiffness as it produces the least amount of error between the true and measured lesion



stiffness ratios which confirms the notion that the shear wave needs some time to become fully developed as it travels through the tissue. Since the error between lesion offsets of 1.25 cm and 2.50 cm is nearly negligible, it is likely that the wave is able to become fully developed even earlier than 2.50 cm and lesion offsets as small as 1.25 cm may be used. The relatively large error present for the largest lesion offset of 3.75 cm is largely due to the severe underestimation of the lesion stiffness for the stiffest lesion seen in Fig. 5.10.

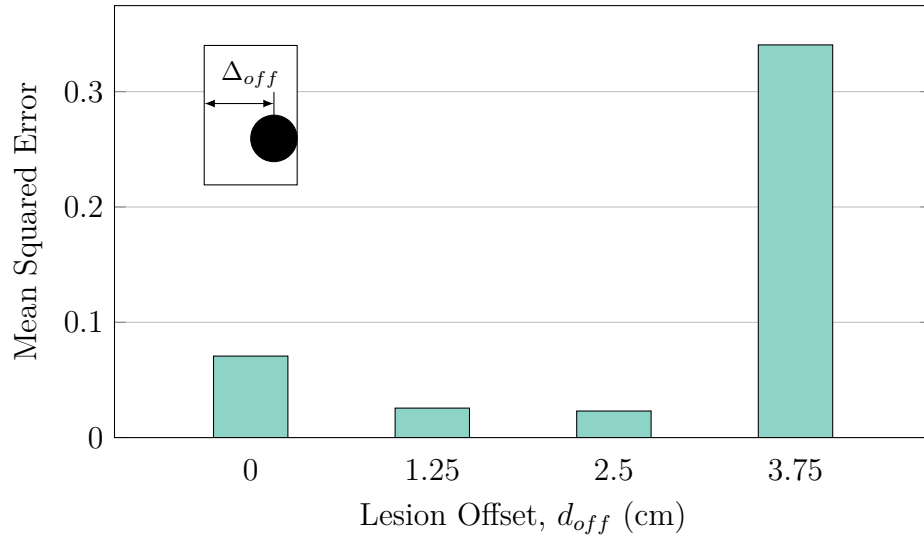


**Fig. 5.11:** Mean squared error between the true and measured lesion stiffness ratios for increasing lesion offsets for a hard-boundaried 0.5 cm radius lesion at a depth of 4 cm using an ARFI interrogation frequency of 2 MHz.

Another key parameter relating to the detection of deep tissue injury lesions relates to the depth that the lesions may actually be detected—for example, in people with large amounts of body fat or muscle, the distance between the surface of the skin and the boney prominence where lesions are most likely to form may be very large compared to someone with very little amounts of body fat or muscle. In order to study the effect of lesion depth on the detection sensitivity of shear wave speed quantification, simulated lesions were placed at

various depths ranging from 2 cm – 8 cm below the surface of the skin with the measured stiffness ratios for these lesions calculated and shown in Fig. 5.12.

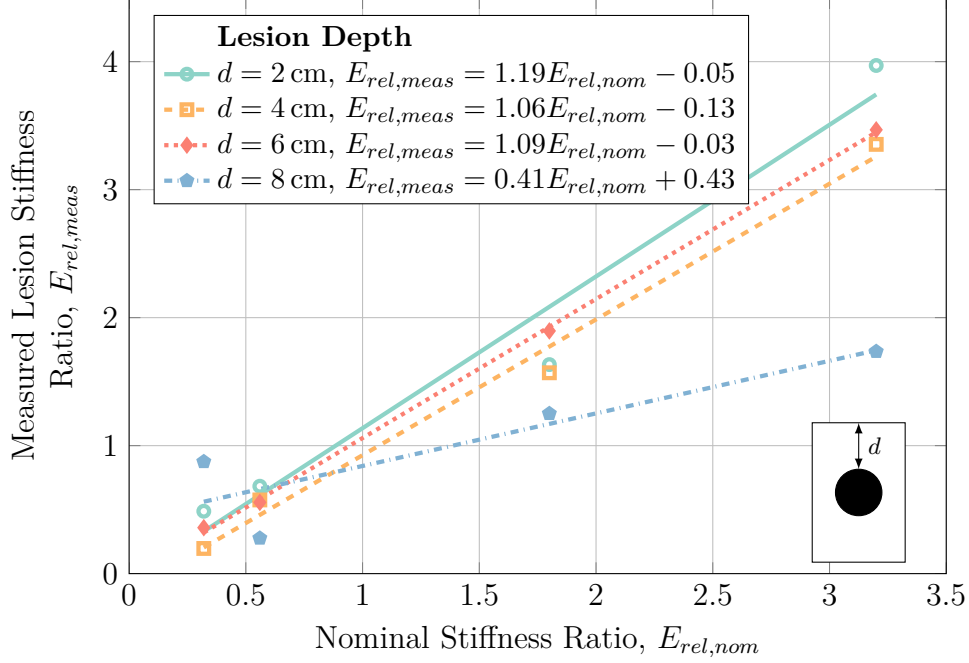


**Fig. 5.12:** Numerical characterization of the shear wave speed measured stiffness ratios acquired with varying lesion and focal point depths for a hard-boundaried 0.5 cm radius lesion with an offset of 2.50 cm using an ARFI interrogation frequency of 2 MHz.

As Fig. 5.12 shows, there is little dependence of shear wave speed quantifications detection sensitivity for shallow to medium-depth lesions—lesions placed at a depth of 2 cm – 6 cm presented approximately equal detection curves. Of note in Fig. 5.12 is that deep lesions—lesions at a depth of 8 cm or more—are difficult to detect as the method is not very sensitive to these deeper lesions—both underestimating the stiffness of deep stiff lesions and overestimating the stiffness of deep unstiff lesions. The large error involved with attempting to measure the stiffness of deep lesions can be seen in Fig. 5.13 where the mean squared error for the various depths examined was calculated. In Fig. 5.13, the 8 cm deep lesions present a significantly greater amount

of error than their shallower counterparts. Also of note is that the shallowest lesions investigated—lesions at a depth of 2 cm—presented with greater error than the mid-depth lesions. The source of this error largely lies in the over-estimation of the stiff lesion stiffness seen in Fig. 5.12 which may be due to numerical errors in the models and calculations.

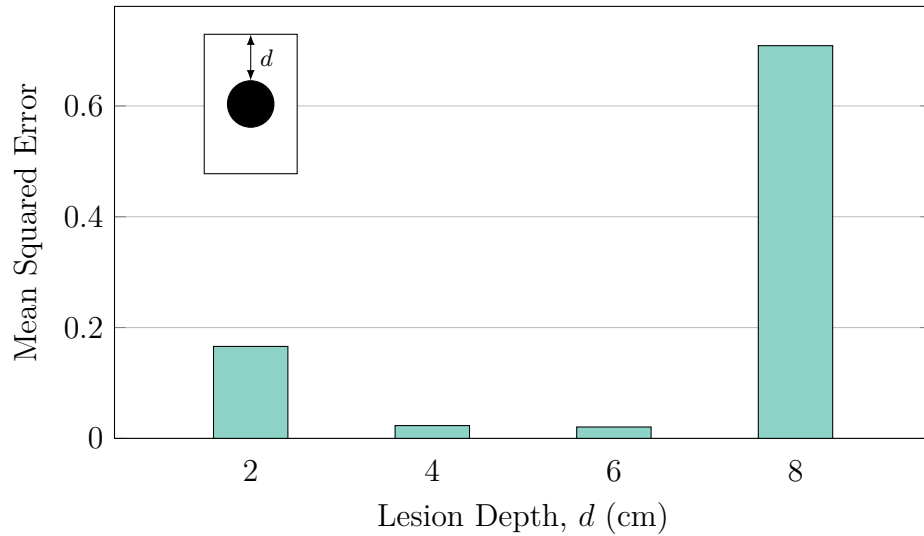


**Fig. 5.13:** Mean squared error between the true and measured lesion stiffness ratios for increasing lesion depths for a hard-boundaried 0.5 cm radius lesion with an offset of 2.50 cm using an ARFI interrogation frequency of 2 MHz.

Since deep tissue injury lesions are unlikely to be perfectly round and hard-boundaried, three different models of lesion geometry were investigated—namely, lesions with blurred boundaries that “fade” into the surrounding tissue, clusters of small lesions that together make up a larger lesions region, and a lesion with MRI-acquired geometry [67] embedded in geometry obtained from a Visible Human slice [126]. Although the spherical hard-boundaried lesions may not represent all the intricacies of real deep tissue injuries, the general trends that result from analysing them may improve the general understanding of lesion detection behaviour.

In order to investigate the effect of blurring lesions into the background tissue, hard-boundaried spherical lesions were blurred with varying blur radii as described in Section 5.2.2. The results of this characterization are presented in Fig. 5.14. As can be seen in Fig. 5.14, the effect of blur radii on lesion detection ability is negligible as noted by how the detection curves of the lesions with varying blur radii are largely coincident.

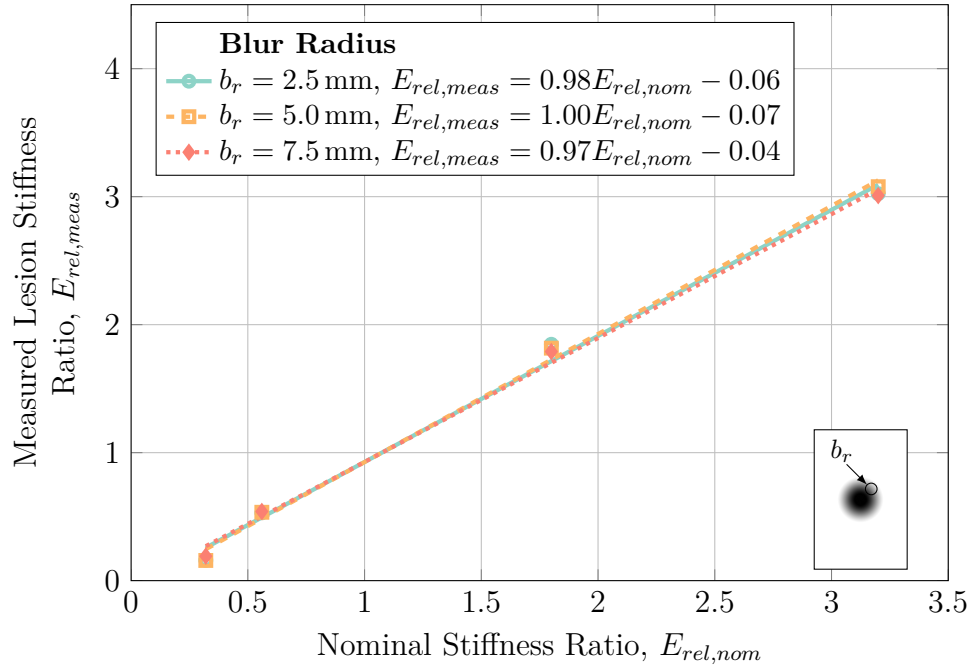


**Fig. 5.14:** Numerical characterization of the shear wave speed measured stiffness ratios acquired with varying lesion and focal point depths for a blurred 1.0 cm radius lesion with an offset of 1.25 cm at a depth of 4 cm using an ARFI interrogation frequency of 2 MHz.

This lack of reliance of detection sensitivity on blur radius is further portrayed by the mean squared error of the results, calculated in Fig. 5.15. While there are some minor differences in the error between the various blur radii—chiefly between blur radii of 2.5 mm and 5.0 mm—the scale of these differences lie within the range of numerical error and noise and so are not significant.

The fact that detection sensitivity does not decrease with increasing blur

radii in shear wave speed quantification makes shear wave speed quantification a desirable tool for detecting deep tissue injury lesions as it means that even imperfect, newly-forming lesions can still be readily detected and monitored.

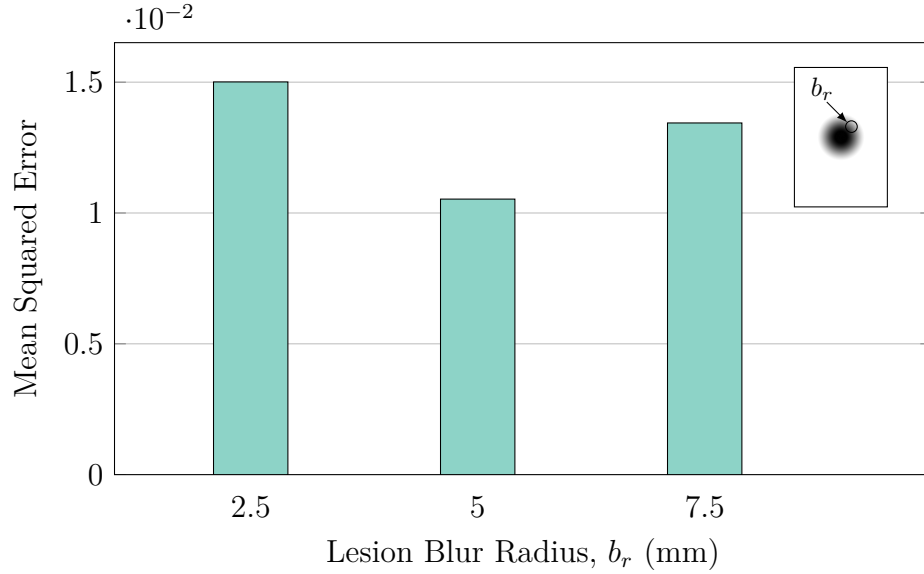


**Fig. 5.15:** Mean squared error between the true and measured lesion stiffness ratios for increasing lesion depths for a blurred 1.0 cm radius lesion with an offset of 1.25 cm at a depth of 4 cm using an ARFI interrogation frequency of 2 MHz.

Beyond having boundaries that “fade” into the background tissue, deep tissue injury lesions may in fact be heterogeneous in nature with a large number of small lesions clustered together to form a larger lesionous region. To investigate this phenomenon, the effect of small clustered lesion density and individual radii were investigated using shear wave speed quantification. The effect of clustered lesion density was investigated as outlined in Section 5.2.2, the results of which are shown in Fig. 5.16.

As Fig. 5.16 shows, decreasing the cluster density generally results in a decreasing detection sensitivity with the least dense clusters both underestimating the stiffness of stiff lesions and overestimating the stiffness of unstiff lesions. This behaviour is somewhat expected—as the density of clustered le-

sions decreases, so too does the mean true stiffness of the lesionous region that is inspected due to the greater ratio of “healthy” tissue to lesionous tissue.

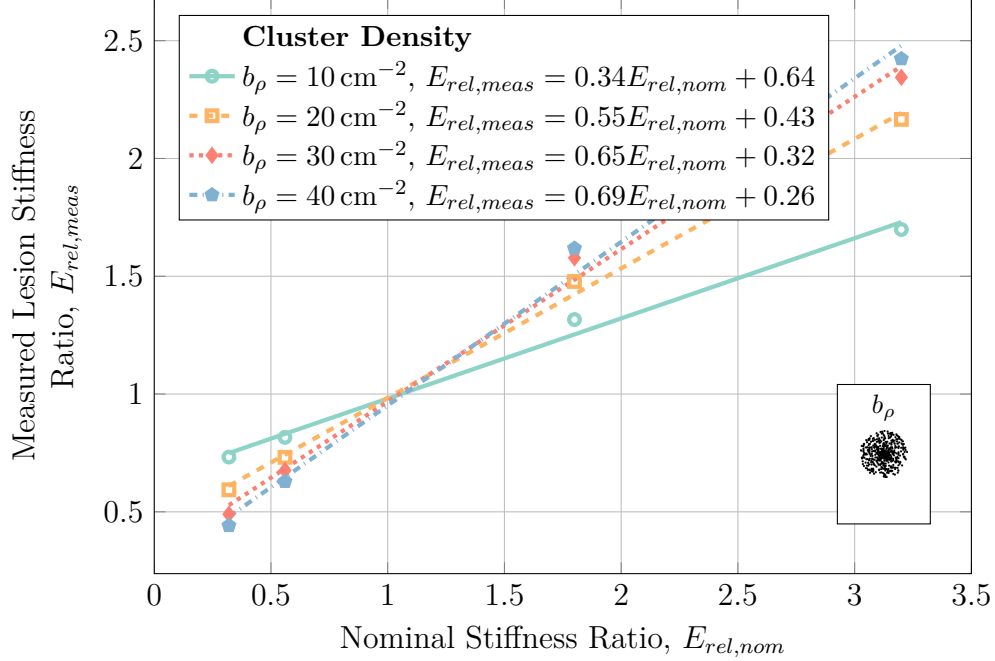


**Fig. 5.16:** Numerical characterization of the shear wave speed measured stiffness ratios acquired with varying cluster densities for clustered 1 mm radius lesions within a 1.0 cm radius with an offset of 1.25 cm at a depth of 4 cm using an ARFI interrogation frequency of 2 MHz.

This generalization is further portrayed by the mean squared error which is shown in Fig. 5.17. In Fig. 5.17, increasing cluster density results in monotonically decreasing error.

Beyond the cluster density, the size of individual clustered lesions within the lesionous region may affect the detection sensitivity. To investigate this parameter, the radii of the individual lesions in the clustered lesion model were varied, with the results presented in Fig. 5.18. Fig. 5.18 shows how decreasing the individual clustered lesion radii results in decreases in the detection sensitivity. This is similar to the results presented in Fig. 5.16 in that decreasing the individual lesion radii results in a decrease of the ratio between lesionous

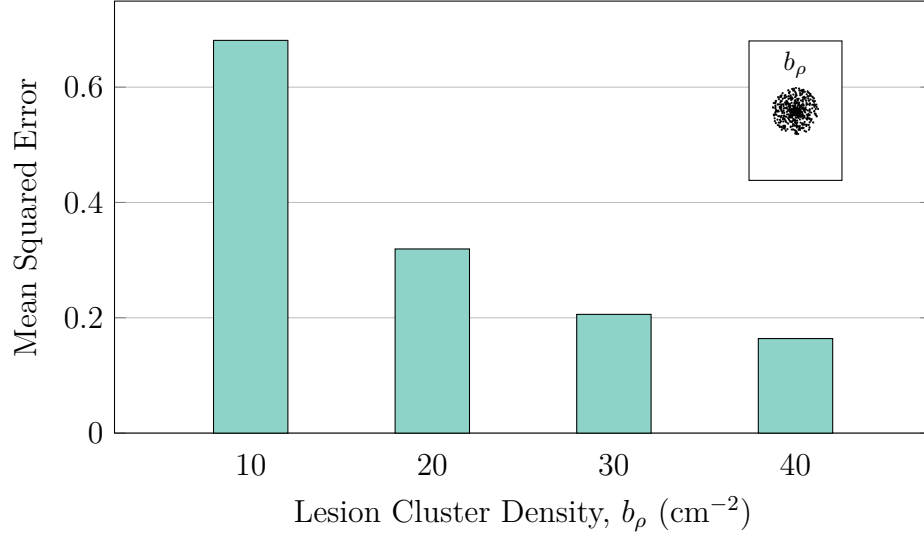


**Fig. 5.17:** Mean squared error between the true and measured lesion stiffness ratios for increasing lesion cluster density for clustered 1 mm radius lesions within a 1.0 cm radius with an offset of 1.25 cm at a depth of 4 cm using an ARFI interrogation frequency of 2 MHz.

tissue and healthy tissue within the lesionous region—the greater the proportion of lesionous tissue within the investigated region, the more accurate the detection of the lesionous region.

Again, this conclusion is corroborated by the mean squared error shown in Fig. 5.19. In Fig. 5.19, increasing the individual lesion radii results in a significant decrease in the stiffness measurement error in the lesionous region.

Finally, in order to place these characterizations within the context of a real deep tissue injury situated within the geometry of a real human soft tissue domain, a numerical characterization of lesion size in the Visible Human lesion model outlined in Section 5.2.2 was carried out with the results portrayed in Fig. 5.20. Fig. 5.20 relates the change in detection sensitivity with different sized lesions and shows that small lesions (with “radii”  $\leq 5.0$  mm) are extremely difficult to detect as the stiffness of small stiff lesions is severely un-

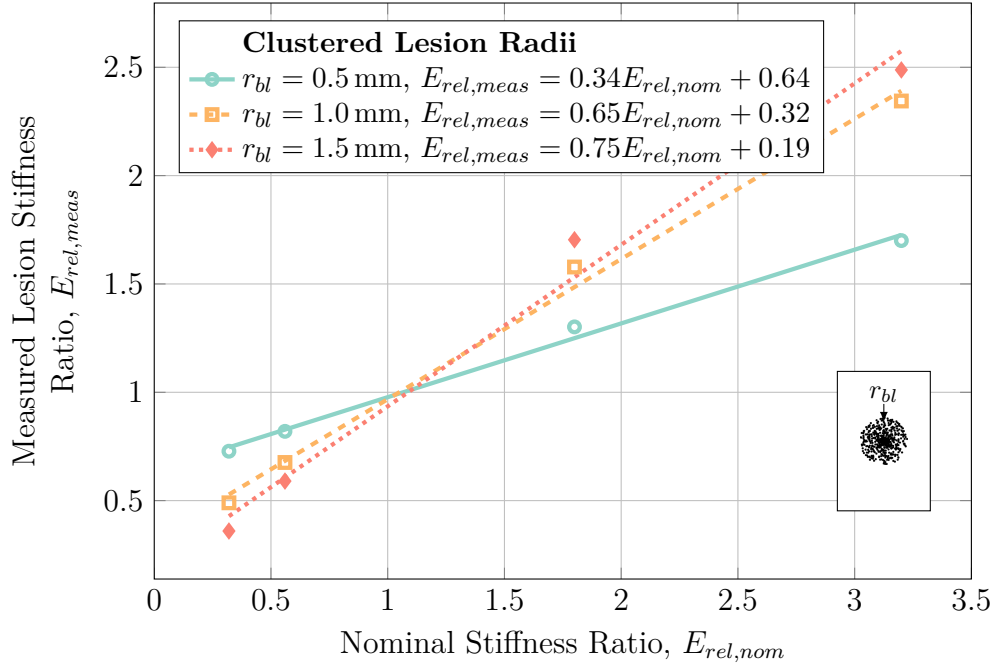


**Fig. 5.18:** Numerical characterization of the shear wave speed measured stiffness ratios acquired with varying clustered lesion radii for clustered lesions with a density of  $30 \text{ cm}^{-2}$  within a  $1.0 \text{ cm}$  radius with an offset of  $1.25 \text{ cm}$  at a depth of  $4 \text{ cm}$  using an ARFI interrogation frequency of  $2 \text{ MHz}$ .

derestimated and the stiffness of small unstiff lesions is severely overestimated. These results align with what was seen in the spherical hard-boundaried lesion case presented in Fig. 5.8, indicating that the simplified spherical results generally hold true for the more complex geometry results.

As expected from the results in Fig. 5.20, increasing the lesion radius results in monotonically decreasing measurement error as is shown in Fig. 5.21 with the least amount of measurement error present for the largest lesions. This means that relatively larger lesions will be easier to detect and accurately quantify and may be due to the shear wave requiring some finite period of time to speed up or slow down with a lesionous region of tissue as discussed previously.

Numerical values for the characterization plots presented here are given in



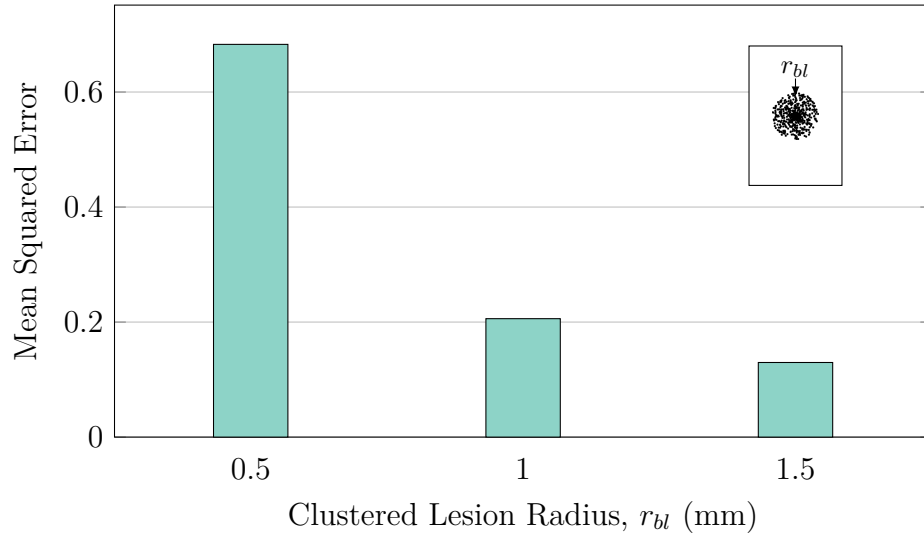


**Fig. 5.19:** Mean squared error between the true and measured lesion stiffness ratios for increasing clustered lesion radii for clustered lesions with a density of  $30 \text{ cm}^{-2}$  within a 1.0 cm radius with an offset of 1.25 cm at a depth of 4 cm using an ARFI interrogation frequency of 2 MHz.

Section A.3 of Appendix A.

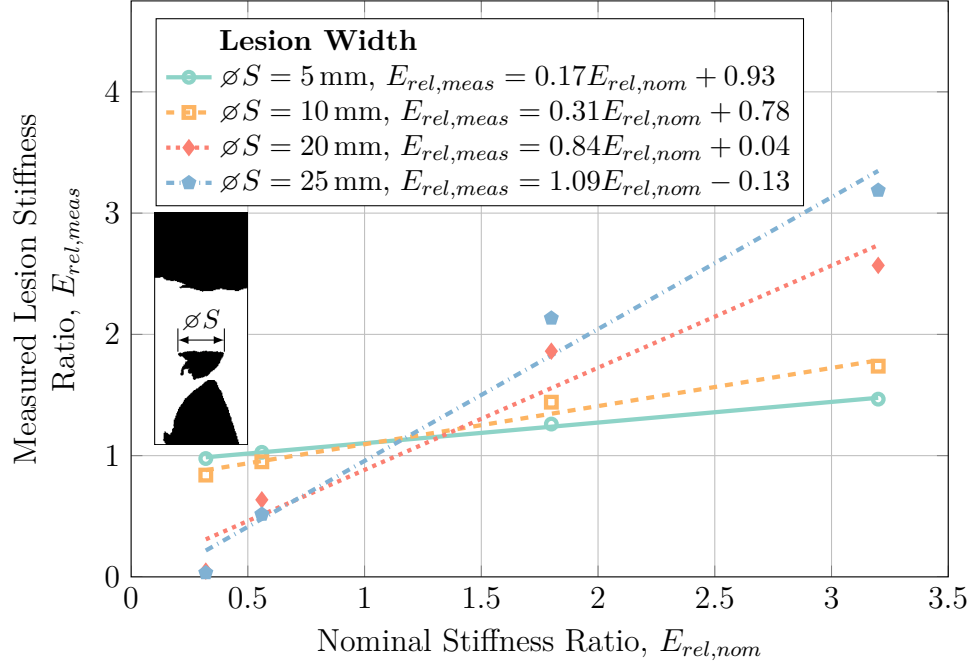


**Fig. 5.20:** Numerical characterization of shear wave speed measured stiffness ratio with changing lesion radii for MRI-acquired lesion geometry in a Visible Human model with an offset of 1.25 cm at a depth of 6 cm using an ARFI interrogation frequency of 2 MHz.

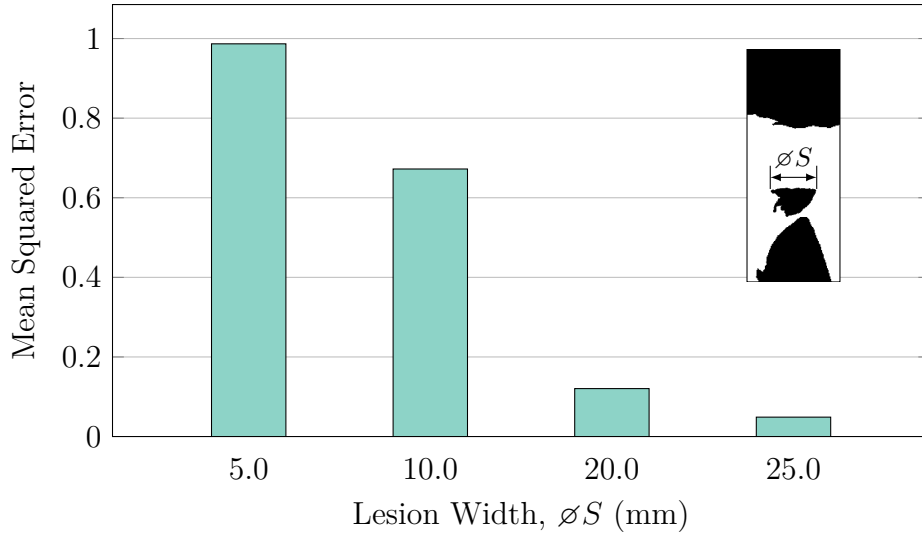


**Fig. 5.21:** Mean squared error between the true and measured lesion stiffness ratios for increasing lesion radii for MRI-acquired lesion geometry in a Visible Human model with an offset of 1.25 cm at a depth of 6 cm using an ARFI interrogation frequency of 2 MHz.

### 5.3.4 Physical Phantom Validation

In order to examine the validity of the simulations presented in Section 5.2.2 and the results presented in Section 5.3, experiments using a physical tissue mimicking phantom and an ultrasound machine were performed as described in Section 5.2.3. The results of these experiments are presented in Figs. 5.22 and 5.23 where the difference between the experimentally measured stiffness ratios of lesions were compared against their nominal and simulated stiffnesses respectively.

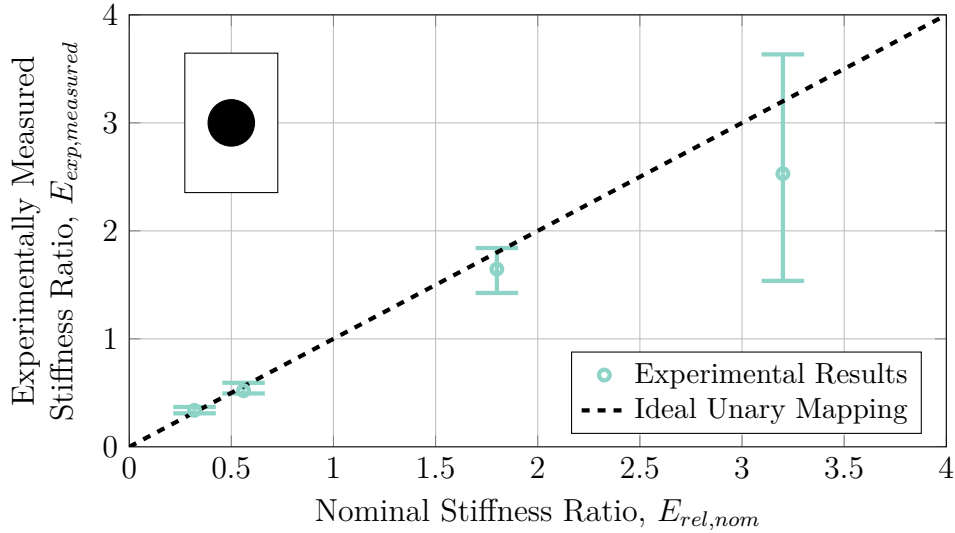


**Fig. 5.22:** Relation between nominally reported strain ratios of the tissue mimicking phantom and experimentally measured strain ratios for a lesion at a depth of 3.5 cm and diameter of 2.0 cm showing general agreement between simulated and experimental cases. Error bars represent the range of measurements acquired.

Fig. 5.22 shows the general agreement between the nominal and experimentally acquired lesion stiffness ratios. Of note is the increasing amount of measurement error associated with increasing nominal stiffness ratios and reflects the general underestimation of stiff lesion stiffness that was seen in the characterization of nearly all stiff lesions in Section 5.3. Further, the relatively

large degree of error was due to the measurement of the shear wave speed within the lesion rather than variability in the shear wave speed of the surrounding tissue. Nonetheless, the experimentally-acquired values lay within error of the expected nominal stiffness ratios, so the experiment was considered to produce acceptable results to compare against the simulations. The results of this comparison are shown in Fig. 5.23 where the stiffness ratios acquired through simulation are compared against experimentally-acquired stiffness ratios of parametrically identical lesions.

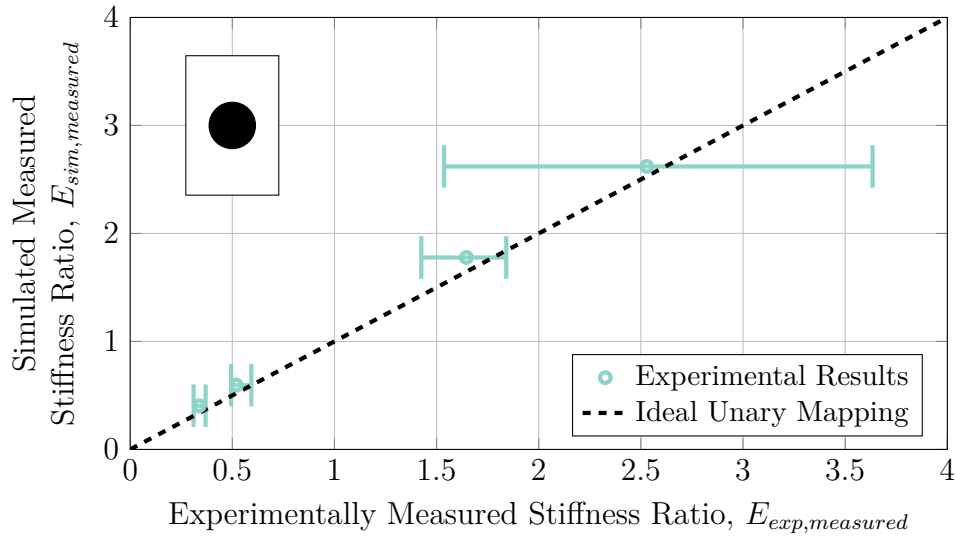


**Fig. 5.23:** Relation between simulated measured strain ratios and experimental measured strain ratios for a lesion at a depth of 3.5cm and diameter of 2.0cm showing general agreement between simulated and experimental cases.

As expected, there is nearly a one-to-one correspondence between the experimentally measured lesion stiffness ratios and the simulated lesion stiffness ratios for the various lesions investigated. In all of the lesion cases studied, the simulated lesion stiffness ratio was slightly greater than the experimentally measured stiffness ratio. This suggests that the simulated models introduce a minor bias in the results, although as the correlation is linear this may be